JACS
JOURNAL OF THE AMERICAN CHEMICAL SOCIETY
pubs.acs.org/JACS
Article

Quantum Shell in a Shell: Engineering Colloidal Nanocrystals for a High-Intensity Excitation Regime

Dulanjan Harankahage, James Cassidy, Jacob Beavon, Jiamin Huang, Niamh Brown, David B. Berkinsky, Andrew Marder, Barbra Kayira, Michael Montemurri, Pavel Anzenbacher, Richard D. Schaller, Liangfeng Sun, Moungi G. Bawendi, Anton V. Malko, Benjamin T. Diroll, and Mikhail Zamkov*

Cite This: J. Am. Chem. Soc. 2023, 145, 13326−13334
Read Online
ACCESS | Metrics & More | Article Recommendations | Supporting Information

ABSTRACT: Many optoelectronic processes in colloidal semiconductor nanocrystals (NCs) suffer an efficiency decline under high-intensity excitation. This issue is caused by Auger recombination of multiple excitons, which converts the NC energy into excess heat, reducing the efficiency and life span of NC-based devices, including photodetectors, X-ray scintillators, lasers, and high-brightness light-emitting diodes (LEDs). Recently, semiconductor quantum shells (QSs) have emerged as a promising NC geometry for the suppression of Auger decay; however, their optoelectronic performance has been hindered by surface-related carrier losses. Here, we address this issue by introducing quantum shells with a CdS−CdSe−CdS−ZnS core−shell−shell−shell multilayer structure. The ZnS barrier inhibits the surface carrier decay, which increases the photoluminescence (PL) quantum yield (QY) to 90% while retaining a high biexciton emission QY of 79%. The improved QS morphology allows demonstrating one of the longest Auger lifetimes reported for colloidal NCs to date. The reduction of nonradiative losses in QSs also leads to suppressed blinking in single nanoparticles and low-threshold amplified spontaneous emission. We expect that ZnS-encapsulated quantum shells will benefit many applications exploiting high-power optical or electrical excitation regimes.

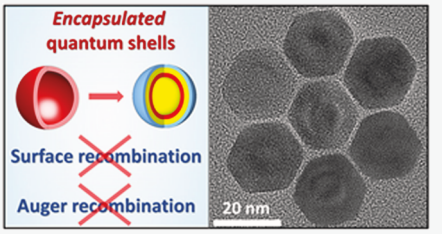

INTRODUCTION

Colloidal semiconductor nanocrystals (NCs) have become increasingly attractive due to their size-tunable band gap and high photoluminescence (PL) quantum yield (QY).[1−7] The PL QY of colloidal NCs, however, declines with increasing excitation intensity. This is caused by the interaction of multiple electron−hole pairs (excitons) within the same nanoparticle that leads to their nonradiative Auger recombination.[8−10] Generally, when multiple excitons per particle are created, Auger recombination becomes the main factor limiting the overall quantum efficiency of optoelectronic processes in NCs.[11] This presents a significant issue for NC applications operating in a multiexciton regime, which include X-ray scintillators,[12,13] high-brightness quantum dot (QD)-LEDs,[14] NC-based light amplification media,[15,16] solar concentrators,[17] and single-dot bio-imaging and tracking.[18]

Compared to zero-dimensional (0D) QDs, 1D−2D colloidal semiconductor NCs exhibit a slower rate of Auger recombination.[19−23] A particularly notable example in this regard is a 2D nanoplatelet geometry[24] (e.g., CdS/CdSe/CdS core−shell or core−crown nanoplatelets), for which the quantum yield of biexciton emission can reach unity. Such remarkable performance can be attributed to two unique characteristics of 2D nanoplatelets: (1) a relaxed carrier confinement in the two spatial dimensions, which reduces exciton−exciton Coulomb interactions, and (2) a relatively fast rate of radiative recombination, which outpaces an already slow Auger decay. The drawback of the 2D nanoplatelet geometry concerns an attractive interaction between excitons, which prevents multiple excitons from utilizing the entire volume of the structure. Not surprisingly, Auger lifetimes of NPLs (0.3−0.5 ns) are lower than expected of such a 2D confinement and are comparable to those of quasi-0D QDs. Furthermore, the fast radiative decay in NPLs, which contributes to a high biexciton QY, can also cause short-lived optical gain in these nanomaterials. This could pose potential problems for optical gain applications since the threshold for both optical and electrical injection is inversely proportional to the biexciton lifetime.[25]

Similar to nanoplatelets, quantum shells[26−31] offer a relaxed carrier confinement in two dimensions but with repulsive rather than attractive interactions between multiple excitons. The exciton−exciton repulsion (positive binding energy) leads to increased spatial dispersion of excitons and therefore reduced rate of their Auger recombination, as was previously demonstrated for CdS−CdSe−CdS core−shell−shell QSs. The biexciton to exciton quantum yield ratio for these materials, QY_{XX}/QY_X, lies in the range of 0.60−0.80, and

Received: April 1, 2023
Published: June 6, 2023

https://doi.org/10.1021/jacs.3c03397
J. Am. Chem. Soc. 2023, 145, 13326−13334

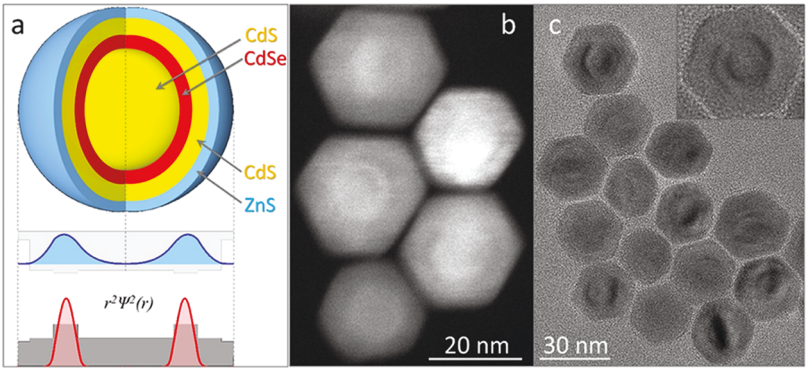

Figure 1. (a) Schematic geometry of a CdS_{bulk}−CdSe−CdS−ZnS quantum shell. The graph shows calculated radial probability distributions of electron and hole wave functions in each region. (b) High-angle annular dark-field (HAADF)-STEM image of 7.2-nm-core quantum shells, illustrating the presence of the CdSe shell layer. (c) TEM image of 9.0-nm-core CdS_{bulk}−CdSe−CdS−ZnS QSs. Inset: High-resolution TEM image of a 9.0-nm-core QS.

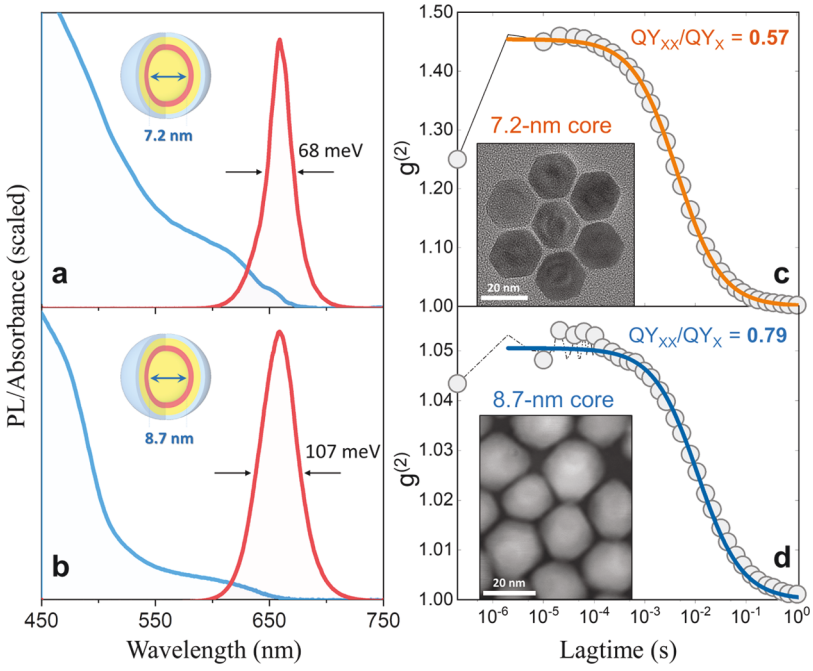

Figure 2. (a) Absorption and emission spectra of 7.2-nm-core CdS_{bulk}−CdSe−CdS−ZnS QSs (R_{CdS} = 3.0 nm, $H_{Se} \approx$ 1.8 nm, $H_{CdS} \approx$ 3.8 nm, and H_{ZnS} < 1.5 nm). (b) Absorption and emission spectra of 8.7-nm-core CdS_{bulk}−CdSe−CdS−ZnS QSs (R_{CdS} = 4.3 nm, $H_{Se} \approx$ 1.8 nm, $H_{CdS} \approx$ 4.2 nm, and H_{ZnS} < 1.5 nm). (c, d) Lagtime dependence of the cross-correlation function, $g^{(2)}$, that was used to determine the ratio of biexciton to exciton QY (QY_{XX}/QY_X) for (c) 7.2-nm core QSs and (d) 8.7-nm core QSs. The displayed cross-correlation function represents the integrated intensity of the correlation peak as detailed in ref 45.

even reaches unity for large core QSs.[32] This indicates a strong suppression of Auger processes. However, the nonradiative decay in QSs is also contributed by the carrier recombination on surfaces and defects. These processes are usually manageable in 0D QDs through surface passivation, but are more pervasive in a QS morphology, limiting PL QY. Long radiative lifetimes of QSs and the delocalization of an electron wave function toward the surface are the primary reasons for such nonradiative losses. Since optoelectronic applications of colloidal NCs often require PL QY in excess of 90%, the geometry of QSs needs to be improved to combat this issue.

Here, we report on the synthesis of CdS−CdSe−CdS−ZnS core−shell−shell−shell colloidal QSs that allow for the suppression of both Auger and surface-related nonradiative recombination processes (Figures 1 and S1). The reported QS morphology enables excellent optical performance over a broad range of excitation intensities, with a PL QY of 90% and biexciton emission QY of up to 79%. Notably, the biexciton Auger lifetime of fabricated QSs ($\tau_{2,Auger}$ = 22−110 ns) was found to exceed those of other nanocrystal geometries by an order of magnitude. Furthermore, the rates of Auger decay in QSs increased more slowly with the number of excitons per particle than in 0D quantum dots, making QSs particularly well suited for multicarrier optoelectronic applications. We demonstrate that the suppression of nonradiative decay in QSs gives rise to a low-threshold amplified spontaneous emission (ASE), suppressed blinking in single nanoparticles, and Auger-inactive single-exciton optical gain.

RESULTS AND DISCUSSION

The geometry of a CdS_{bulk}−CdSe−CdS−ZnS QS is illustrated in Figure 1a. This structure is derived from previously reported

https://doi.org/10.1021/jacs.3c03397
J. Am. Chem. Soc. 2023, 145, 13326−13334

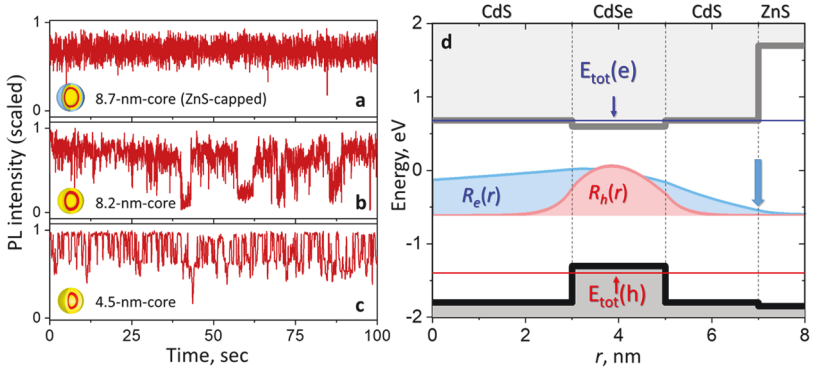

Figure 3. Representative PL intensity trajectories of single quantum shells: (a) 8.7-nm-core CdS_{bulk}−CdSe−CdS−ZnS QS, (b) 8.2-nm-core CdS_{bulk}−CdSe−CdS QS, and (c) 4.5-nm-core CdS_{bulk}−CdSe−CdS QS. (d) Calculated electron and hole radial wave functions for lowest-energy excited states in a CdS_{bulk}−CdSe−CdS−ZnS quantum shell (R_{CdS} = 3.0 nm, H_{CdSe} = 2 nm, H_{CdS} = 2 nm, H_{ZnS} = 1 nm). The possibility of quantum shell clustering was excluded by measuring the gate time dependence of $g^{(2)}$ in Figure S8. The conduction and valence band energies as well as the ground-state energies, $E_{e,1s}$ and $E_{h,1s}$, are also shown. The blue arrow marks the CdS/ZnS interface, where $R_e(r) \neq 0$.

quantum-dot quantum wells (QDQW)[33−39] and consists of a CdSe quantum-well layer sandwiched between the core and the shell CdS "barrier" components. The incorporation of a large CdS core component in QSs increases the volume of the CdSe quantum-well layer, which, in turn, reduces the rate of multiexciton Auger recombination ($k^{-1} \sim V^{1.1}$).[40,41] The relative positions of conduction and valence energies at QS interfaces lead to a strong radial confinement of holes within the CdSe quantum well. Conversely, electrons are more delocalized in the radial direction but have minimal coupling to surface states due to the presence of the ZnS shell (Figure 1a).

Recent progress in the synthesis of CdSe-based quantum shells has been driven by the need to address the low PL QY and broad emission linewidths reported in early works.[42] The challenge has been to adequately passivate the surface of quantum shells without introducing a lattice strain. In the present study, this goal was achieved by employing CdS−ZnS interfacial alloying, which allowed for a substantial increase in the PL QY without the reduction of multiexciton lifetimes.

The four-step synthesis of CdS_{bulk}−CdSe−CdS−ZnS QSs is described in the Experimental Section. Briefly, large-size CdS core nanoparticles were synthesized using an aggregative growth strategy.[43] This method employs a thermodynamic growth regime, which naturally leads to size focusing with reaction time. In the case of large-size colloids, it was found to be more effective both in terms of speed and product homogeneity than a conventional, precursor-based, kinetic growth. Aggregative growth was particularly beneficial in the case of nanostructures with diameters greater than 8 nm, where the particle size dispersion was as low as 5% (Figures S2 and S3). Second, the growth of the CdSe layer was performed in the presence of dioctylamine. This approach was encouraged by an earlier study[44] demonstrating that secondary amines, such as dioctylamine, can reduce the occurrence of postnucleation during shell growth. Finally, all three shell layers were deposited using a slow injection of precursors by means of two separate syringe pumps. An example of PL spectral evolution corresponding to the four sequential stages of the QS growth is shown in Figure S5a−d.

In Figure 2, we compare the two types of CdS_{bulk}−CdSe−CdS−ZnS QSs with CdS core sizes of 7.2 nm (Figure 2a) and 8.7 nm (Figure 2b). The 7.2-nm-core QSs exhibited a narrow emission linewidth of 68 meV with a corresponding photoluminescence (PL) quantum yield (QY) of 78%. The 8.7-nm-core sample had a broader PL spectrum (linewidth of 107 meV) and a PL QY of 90%. Generally, it remains challenging to achieve a high PL QY while maintaining a narrow PL linewidth, since the former characteristic requires interfacial alloying that naturally broadens the emission peak.

The quantum yield of biexciton emission in fabricated QSs was measured by means of fluorescence correlation spectroscopy.[45] A Hanbury−Brown−Twiss setup, comprising a confocal microscope and a pulsed excitation source, was used to collect emission from diffusing nanoparticles in solution. The second-order cross-correlation function, $g^{(2)}(\tau)$, was calculated according to the protocol outlined in the Supporting Information, Section II. Figure 2c,d shows that the QY_{XX}/QY_X is higher for the 8.7-nm-core QDs (78.6 ± 0.017%) compared to 7.2-nm-core samples (56.8 ± 0.016%), suggesting a reduction in the nonradiative Auger recombination pathway as a function of the core diameter. The increase in the value of QY_{XX}/QY_X with the size of the QS core has been observed previously and was explained as due to the increased exciton volume of larger-core QSs.[29,32] We note that the biexciton QY of zero-dimensional CdSe/CdS core/shell QDs is usually lower, QY_{XX}/QY_X = 10−40%.[45−48]

The insets in Figure 2c,d show characteristic TEM/STEM images of fabricated QSs. The total diameter of 7.2-nm-core QSs was determined to be 20.1 nm, while 8.7-nm-core QSs averaged about 21.2 nm in size. The location of the CdSe quantum well layer can be distinguished for both types of QSs. The lattice structure of fabricated samples was wurtzite (Figure S4), with diffraction peaks indexed primarily to hexagonal CdS.

Single-particle PL measurements further elucidate the role of the quantum shell geometry in suppressing the nonradiative carrier recombination. Figure 3a−c demonstrates representative PL blinking traces of three QSs: (a) 8.7-nm-core CdS_{bulk}−CdSe−CdS−ZnS QSs, (b) 8.2-nm-core CdS_{bulk}−CdSe−CdS QSs, and (c) 4.5-nm-core CdS_{bulk}−CdSe−CdS QSs. The most significant blinking (PL alternating between bright and gray states) was observed in samples with the smallest, 4.5-nm CdS core and CdS-only surface layer. Samples with a larger, 8.2-nm core and CdS-only surface layer showed a reduction in the frequency of a "gray" state. Finally, the 8.7-nm-core sample with a composite CdS−ZnS surface layer had no apparent blinking. Similar nonblinking behavior was observed across several ZnS-capped QSs (Figure S7). By comparing samples (a) and (b), we conclude that the presence of ZnS capping

https://doi.org/10.1021/jacs.3c03397
J. Am. Chem. Soc. 2023, 145, 13326−13334

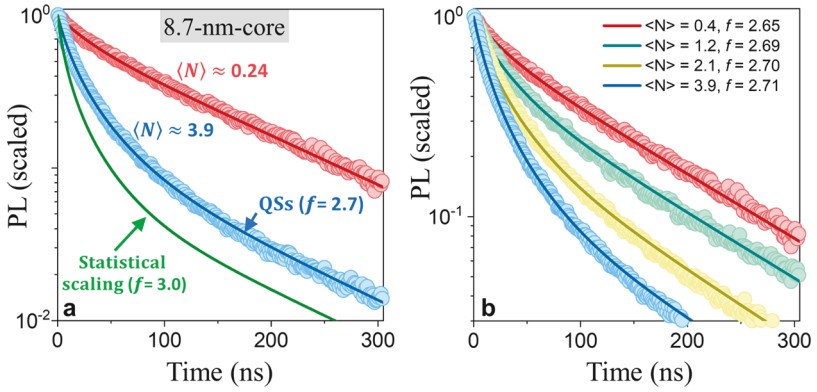

Figure 4. (a) PL intensity decay of 8.7-nm-core QSs resulting from two excitation regimes: low-power, $\langle N_{eh}\rangle$ = 0.24 (red circles) and high-power, $\langle N_{eh}\rangle$ = 3.9 (blue circles). The blue curve represents a fit using a parametric model curve (eq 1). The best fit is obtained using f = 2.7, which deviates from the statistical scaling of multiexciton rates (f = 3.0, green curve). (b) PL intensity decay of 8.7-nm-core QSs resulting from a range of excitation powers, corresponding to $\langle N_{eh}\rangle$ = 0.4−3.9. The fitting parameter for each case is shown in the legend.

layer plays an important role in reducing blinking. This was attributed to the suppression of carrier surface recombination in ZnS-capped QSs. Furthermore, based on the comparison of samples (b) and (c), we conclude that increasing the size of the core also appears to play a role in blinking suppression. We attribute the latter phenomenon to the reduction of Auger rates in larger-core QSs, which diminishes the likelihood of charged excitons.[49]

An important role of the ZnS shell in improving the PL QY of QSs has also been confirmed theoretically through calculation of zero-angular momentum electronic wave functions within the effective mass approximation.[50] The details of these calculations are given in the Supporting Information, Section III. Figure 3d shows the radial wave function for the lowest-energy electron and hole states of a quantum shell. The wave function of a hole is localized within the CdSe shell layer. Conversely, an electron wave function is delocalized such that its amplitude does not vanish at the interface of CdS and ZnS. This suggests that for QSs with CdS-only surface, electrons could interact with surface states, resulting in nonradiative decay of excitons.

Achieving long Auger lifetimes in QSs can improve the efficiency of many optoelectronic processes. Here, we estimate biexciton Auger lifetimes in QSs, $\tau_{2,Auger}$, by using experimental values of $g_{XX} = QY_{XX}/QY_X$ (Figure 2c,d) and PL QY (see Supporting Information, Section I.1)

$$\tau_{2,Auger} = \frac{g_{XX}\tau_X}{\beta(1 - g_{XX}QY_X)} \quad (1)$$

where τ_X is a single-exciton lifetime and β represents the scaling of the biexciton radiative rate relative to that of single excitons. If all deexcitation paths involving the two electron−hole pairs are open, the statistical scaling of radiative rates with the number of electron−hole pairs, m, yields β = 4. Under this assumption, Auger lifetimes of 7.2- and 8.7-nm core QSs are ∼22 and ∼90 ns, respectively (see Table S1). However, it is reasonable to assume that not all electron−hole decay paths are accessible in QSs since repulsive interactions of two electron−hole pairs change the individual e−h recombination probabilities, compared to a single exciton configuration. As a result, multiexciton radiative rates in QSs are likely to deviate from the statistical scaling ($\beta \neq 4$).[49]

To get a more accurate estimate of biexciton Auger lifetimes in QSs, we use a strategy that employs β as a fitting parameter. This method is based on correlating the power dependence of the ensemble PL intensity decay with the average number of excitation photons per particle, $\langle N_{eh}\rangle$. In the present work, $\langle N_{eh}\rangle = f \times \sigma$ is calculated from the QS absorption cross section, σ, and the pump fluence, f, where σ is measured using the analysis presented in ref 51.

For a given $\langle N_{eh}\rangle$, the probability of a QS absorbing m photons, $f(m)$, is estimated using the Poisson distribution: $f(m) = \langle N_{eh}\rangle^m \times e^{-m}/m!$ Considering that Auger decay of an m-exciton state results in a state with $(m - 1)$ excitons, the temporal evolution of the m-exciton population in a QS, $P(m, t)$, is then determined by solving coupled rate equations

$$\frac{dP(m, t)}{dt} = k_{m+1}P(m + 1, t) - k_mP(m, t) \quad (2)$$

where $k_m = k_{m,r} + k_{m,nr}$ represents the total decay rate of an m-exciton state. This model does not account for emissive charged exciton species since they are strongly suppressed, as can be inferred from nearly blinking-free single-particle emission trajectories of ZnS-overcoated QSs (see Figure 3a).

Klimov et al.[52] have analyzed m-scaling for a small number of excitons per nanocrystal using first-order perturbation theory. It was concluded that in the case of symmetric multiexcitons, decay rates scale statistically with the total number of individual transitions, i.e.

$$k_{m,r} = m^2k_{r,2}/4, \quad k_{m,nr} = m^2(m - 1)k_{nr,2}/4 \quad (3)$$

However, for asymmetric multiexcitons comprising both 1S and 1P states or multiexciton populations in large-size nanostructures, the m-scaling is expected to deviate from statistical due to reduced coupling between electron and hole states with different symmetries.[52] Based on these results, we propose that a universal approach to scaling of multiexciton radiative and nonradiative decay rates can be achieved by using a variable power parameter f = 2−3, where f = 3 represents statistical scaling and f = 2 simulates multiexciton behavior in bulk semiconductors, where Auger recombination rates are significantly lower. Under these considerations, the multiexciton decay rates can be parametrized as a function of a single fitting parameter, f (see Supporting Information, Section I.2)

$$k_{m,r} = m^{f-1}k_{r,1} \quad (4)$$

https://doi.org/10.1021/jacs.3c03397
J. Am. Chem. Soc. 2023, 145, 13326−13334

$$k_{m,\mathrm{nr}} = m^f k_{2,\mathrm{nr}}/2^f = \frac{m^f}{2} \times \frac{1 - g_{\mathrm{XX}}\mathrm{QY_1}}{g_{\mathrm{XX}}\mathrm{QY_1}} \times k_{1,\mathrm{r}} \quad (5)$$

Figure 4a shows the PL intensity decay of 8.7-nm-core QSs resulting from low-power and high-power excitation regimes ($\langle N_{\mathrm{eh}}\rangle$ = 0.24 and $\langle N_{\mathrm{eh}}\rangle$ = 3.9, respectively). Measurements corresponding to an intermediate range of excitation powers ($\langle N_{\mathrm{eh}}\rangle$ = 0.24−3.9) are summarized in Figure 4b. A single-parameter fit to the experimental PL decay in Figure 4a (blue curve) is achieved with f = 2.7. For comparison, the PL intensity decay expected from statistical scaling of multiexciton rates (f = 3) is also included. At lower excitation powers, the best parametric fit was observed for f = 2.6−2.8 (Figure 4b).

According to the PL decay fit in Figure 4, multiexciton interactions in QSs deviate from statistical scaling, suggesting that underlying exciton−exciton interactions in QSs are generally weaker than in strongly confined NC geometries. This could be a combined effect of a larger QS volume and a repulsive interaction between excitons in QSs. Indeed, we hypothesize that in large-size QSs, the carrier density resulting from several absorbed photons is relatively low, causing the corresponding reduction in Auger decay rates. This is an important feature of multiexciton interactions in large-volume QSs, which could have important implications for the development of optoelectronic devices.

If we assume f = 2.7 scaling of multiexciton rates in QSs, the corresponding biexciton Auger lifetimes become: $\tau_{2,\mathrm{Auger}}$ = 27.4 ns for the 7.2-nm-core and $\tau_{2,\mathrm{Auger}}$ = 110.2 ns for 8.7-nm-core QSs (Table S2). We note that these are at least an order of magnitude greater than those previously reported for CdSe/CdS core−shell QDs, CdS/CdSe/CdS NPLs, or inorganic halide perovskite QDs.[2] Long Auger lifetimes in QSs offer several important benefits. First, a slow Auger decay enables an efficient energy transfer from the biexciton to the exciton state, which is essential for the realization of high-brightness LEDs, ionizing radiation scintillators, etc. Second, long multiexciton Auger lifetimes reduce heat generation in nanocrystals, which should improve the longevity of related devices under electrical or optical excitation.

The long Auger lifetimes of QSs make them a promising material for solution processing of lasing media. To explore this avenue, we have measured the amplified spontaneous emission (ASE) from solid films of 7.2-nm-core QSs (see Figure 5a). To this end, ultrafast pulses were focused onto a film through a cylindrical lens, resulting in the observation of ASE perpendicular to the excitation beam. The ASE onset was observed as a spectrally narrowed peak with superlinear fluence dependence on the higher-energy side of the broader PL feature. The corresponding energy difference between the PL and ASE peaks is consistent with a biexciton origin of the optical gain that corresponds to the biexciton binding energy of 63 meV (exciton−exciton repulsion). Previously, the exciton−exciton repulsion phenomenon has been observed only in type II nanocrystals,[53] where electrons and holes occupy different material domains of a core−shell nanoparticle. Notably, the biexciton ASE peak in QSs appears at a low pump fluence of 5.3 μJ/cm^2 (Figure 5b).

In addition to the biexciton ASE feature (E = 2.02 eV), another narrow-bandwidth ASE peak is observed at a pump fluence of 6 μJ/cm^2 (Figure 5a). The spectral position of this feature matches the steady-state PL, indicating an exciton origin of the emission. ASE resulting from single-exciton transitions is caused by the exciton−exciton (X−X) repulsion

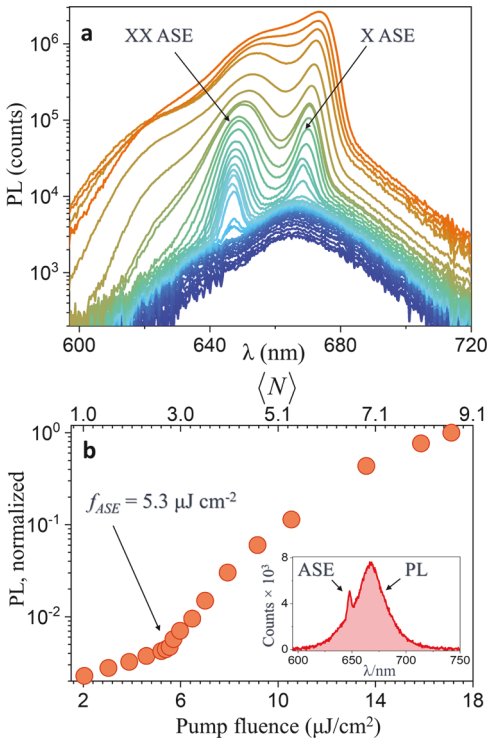

Figure 5. (a) ASE spectra detected from thin films of 7.2-nm-core QSs at different pump fluences. The narrow ASE peak at ∼650 nm corresponds to biexciton optical gain. The onset of the lower-energy ASE peak at ∼670 nm that matches the spectral position of the PL feature is ascribed to a single-exciton gain mechanism. (b) Evolution of the PL intensity for 7.2-nm-core QSs at the spectral position of the biexciton ASE with increasing pump fluence. The corresponding average number of excitons per quantum shell, ⟨N⟩, is shown in the top axis. The ASE threshold is determined to be 5.3 μJ/cm2. The inset shows the onset of biexciton ASE on the high-energy side of the PL peak.

such that the absorption energy of the secondary photon in QSs is perturbed by the X−X interaction.[54] Additionally, the observation of the single-exciton ASE feature at higher fluences than the biexciton ASE feature is likely due to the interaction between the X and X−X emissive phases, as discussed in ref 29. We also note the onset of X and XX ASE features occurs at higher ⟨N⟩ values than expected (Figure 5b, top axis). We have previously investigated this threshold suppression phenomenon in QS films (ref 29) and attributed the enhanced ⟨N⟩ to reabsorption. This phenomenon occurs because the absorption of single-exciton and double-exciton emission in solid films is significant. The reabsorption of emitted photons leads to the suppression of optical gain, thereby enhancing the ASE threshold. We are currently focusing our efforts on improving the quality of QS films to reduce the threshold fluence further.

As the excitation fluence is increased, the exciton and biexciton 1S transitions become saturated, leading to ASE from higher-energy excitons (Figure 5a, $\lambda \approx$ 620 nm). These are likely to involve transitions from 2S and 1P states. It is worth noting that optical gain from 1P excitons is rarely seen in conventional core−shell QDs, as their multiexciton lifetimes are relatively short. Such multiexciton ASE allows for an optical amplification with a wide spectral bandwidth.

https://doi.org/10.1021/jacs.3c03397
J. Am. Chem. Soc. 2023, 145, 13326−13334

CONCLUSIONS

In conclusion, we demonstrate that Auger lifetimes of ZnS-encapsulated quantum shells are significantly longer than those reported for other types of colloidal nanocrystals. Since Auger processes convert optical and/or electrical energy of nanocrystals into excess heat, longer Auger lifetimes imply greater efficiencies and longer thermal stability of devices, including photodetectors/X-ray scintillators, lasers, and high-brightness LEDs. Furthermore, a slow Auger decay enables an efficient energy transfer from the biexciton to the exciton state, which is essential for increasing the PL efficiency in a multiexciton regime. Overall, our findings suggest that the two main mechanisms of nonradiative decay in colloidal nanocrystals, surface recombination and Auger recombination, are suppressed in ZnS-passivated quantum shells. This should encourage the deployment of quantum shells in a variety of applications exploiting high-power optical or electrical excitation regimes.

EXPERIMENTAL SECTION

Materials. The chemicals used in this work were used without any further purification or modification. These chemicals included anhydrous acetone (99%, Amresco), cadmium oxide (CdO, 99.95%, MilliporeSigma), zinc acetate dehydrate (98%, Acros Organics), ethanol (BeanTown Chemical, 99%), hexane (Thermo Scientific), 1-octadecene (ODE, MiliporeSigma 90%), octane (MiliporeSigma 98%), 1-octanethiol (Alfa Aesar, 97%), oleic acid (OA, MiliporeSigma, 90%,), oleylamine (OLAM, MiliporeSigma, 70%,), dioctylamine (DOA, MiliporeSigma, 97%), selenium powder (Se, Thermo Scientific, 99.5%, 200 mesh), sulfur powder (S, Thermo Scientific, 99.999%), toluene (99.8%, MiliporeSigma), and tri-*n*-octylphosphine (TOP, Strem Chemical, 97%).

Synthesis of 6−9-nm Bulk-Size CdS Nanocrystals. Large-size CdS NCs were fabricated using a coalescence-based growth procedure.[55] To this end, 8 mL of OLAM and 42 mg of $CdCl_2$ were added into a 25 mL flask, transferred to an argon atmosphere (using a Schlenk line), and heated to 240 °C. Subsequently, 540 nmol of small-size CdS NCs (2−4 nm diameter) was quickly injected into the flask, resulting in a rapid coalescence growth (about 60 min). The flask was then removed from the heating mantle. The product was then cleaned via precipitation with a toluene/ethanol mixture, as detailed below.

(1) Add an equal volume of EtOH to the nanoparticle solution in a centrifuge tube.
(2) Gently mix the solution by inverting the centrifuge tube twice. Avoid vigorous shaking.
(3) Centrifuge the mixture for 2−3 min at 4500 rpm.
(4) Carefully pour off the supernatant (the liquid on top) without disturbing the nanoparticle pellet (the solid at the bottom of the tube).
(5) Add fresh hexane to the nanoparticle pellet, dissolve it by shaking, and then repeat the washing process (steps (1)−(4)).
(6) After the final wash, remove the supernatant completely and allow the nanoparticle pellet to air dry. Once the pellet is dry, redissolve it in hexane for further use.

The CdS core nanocrystals were then re-capped with OA ligands by dissolving in a mixture of 5 mL of ODE and 8 mL of OA. The flask was again put under the argon and heated to 150 °C for 60 min. The final product was redispersed in hexane and stored under ambient conditions.

Synthesis of CdS_{bulk}−CdSe Core−Shell NCs. The synthesis of the CdSe shell layer was performed by co-injection of the two corresponding precursors (0.1 M Cd-oleate and 0.1 M TOP-Se) via two syringe pumps. The Cd-oleate precursor was made by combining 412 mg of CdO, 8 mL of OA, and 5 mL of ODE in a 50 mL flask and heating the mixture to 260 °C under argon until a clear and nearly colorless solution was obtained. At this point, an additional 19 mL of ODE was injected into the flask. The Se precursor was fabricated by combining 141 mg of Se powder and 3 mL of TOP in a 25 mL flask and heating the mixture to 140 °C under argon until the selenium powder had dissolved. Subsequently, 14 mL of ODE was added to the flask. To initiate the shell growth reaction, 540 or 1080 nmol of CdS NCs were added to a 100 mL flask with 2 mL of dioctylamine (DOA) and 2 mL of ODE. The temperature was set to 110 °C, and the flask was degassed until bubbling had ceased. The flask was then placed under argon and the temperature was set to 315 °C. At 270 °C, the injection of cadmium and selenium precursors was initiated at a rate of 3 mL/h. The injection continued until the PL feature had reached the desired wavelength (usually from 620 to 695 nm). The total injection time was greater for the large-size CdS NCs (∼90 min) than for the medium-size CdS NCs (∼70 min). Once the injection was stopped, the reaction was removed from the heating mantle and cooled to room temperature. To clean the nanoparticle product, we followed the six-step protocol in the previous section.

Synthesis of CdS_{bulk}−CdSe−CdS Core−Shell−Shell NCs. The $Cd(oleate)_2$ solution was fabricated as described in the previous section. The sulfur precursor was prepared by mixing 11.66 mL of ODE and 0.34 mL of octanethiol. The 540 or 1080 nmol of CdS−CdSe core−shell NCs, prepared previously, was loaded into a 100 mL flask with 2 mL of DOA and 2 mL of ODE. The mixture was degassed at 130 °C, transferred to Argon, and heated to 315 °C. The two precursors were injected at a rate of 3 mL/h, starting at 270 °C using separate syringe pumps. The growth reaction usually lasted 2−4 h. Once the injection was finished, the solution was left to anneal for 45 min followed by cooling to room temperature. NC product was then cleaned using a protocol described in the Synthesis of 6−9-nm Bulk-Size CdS Nanocrystals section. The final product was dispersed in hexane.

Deposition of the ZnS Shell via ZnS−CdS Alloying. The ZnS shell was deposited by injection of three precursors (0.1 M TOP-S and a mixture of 0.1 M Cd-Oleate with 0.1 M $Zn(OA)_2$). The Cd-oleate precursor was prepared as before and kept under an argon atmosphere (via a Schlenk line) at 100 °C. The S precursor was made by combining 38.4 mg of S powder and 2 mL of TOP into a 25 mL flask and heating to 140 °C under argon until all of the sulfur powder had reacted, then 10 mL of ODE was injected into the flask to dilute the solution. The $Zn(OA)_2$ was prepared by combining 526 mg of zinc acetate dihydrate with 3 mL of OA and 15 mL of ODE in a 50 mL flask. The flask was then degassed at temperature increments of 60, 80, 100, and 120 °C. Once degassed, the flask was placed in an argon atmosphere and 2 mL of TOP was injected. The temperature was then increased to 240 °C before being cooled and kept at 100 °C. To begin, 540 or 1080 nmol of CdS−CdSe−CdS NCs was loaded into a 100 mL flask with 2 mL of ODE and 2 mL of DOA and degassed at 110 °C. Once finished, the flask was put under argon and the temperature was set to 260 °C. While heating, a 3:1 mL mixture of the Cd and Zn precursors was mixed in a 10 mL flask under argon. This CdZn mixture was then loaded into a syringe and matched in volume with another syringe containing the sulfur precursor. The two precursors were placed in a syringe pump and injected into the flask beginning at 260 °C for 30 min at a rate of 3 mL/h. At this point, the CdZn syringe was removed from the pump, flushed with hexane, and then reloaded with a 2:2 mL mixture of Cd and Zn prepared as the previous mixture. The S syringe was then loaded to match, and the precursors were injected for another 30 min at 3 mL/h. This process was subsequently repeated for a 1:3 mL mixture of Cd and Zn. A final injection of 100% $Zn(OA)_2$ and S-TOP was performed for 40 min. The temperature was raised to 315 °C immediately after this injection began. After the injection finished, 1.5 mL of OA was injected into the flask, and the heating mantle was turned off, allowing for a slow cooldown of the flask. The NCs were precipitated with toluene and a 1:2 mixture of ethanol and acetone *via* centrifugation and dispersed in hexane.

Characterization. The absorbance spectra were obtained using a Cary 60 scan spectrophotometer. For photoluminescence (PL) spectra measurements, a pulsed 405 nm laser diode (PDL 800-D,

https://doi.org/10.1021/jacs.3c03397
J. Am. Chem. Soc. 2023, 145, 13326−13334

Picoquant) was used for excitation, and the emitted photons were collected by a fiber optic cable attached to an Andor Shamrock 303i spectrograph coupled to an Andor Newton 970 EMCCD. TEM images from Thermo Fisher Talos F200X G2 S/TEM were acquired at 200 kV on carbon films coated with a copper grid (300 mesh). The absolute PL QY was measured with the Quantaurus-QY Absolute PL quantum yield spectrometer C11347 (Hamamatsu, Inc., Japan).

Amplified Spontaneous Emission Measurements and Dynamics. To create nanocrystal thin films, an additional antisolvent precipitation with ethanol was carried out, followed by redispersion using a 9:1 hexane/octane mixture. Highly concentrated solutions were drop-cast onto microscope slides treated with MPTS. Samples that displayed the lowest ASE thresholds were subjected to spin coating at 2000 rpm, resulting in glassy, low-scatter films. Other films, however, had perceptible haze and higher thresholds for ASE development. A 35 fs Ti:sapphire laser (with a frequency-doubled to 400 nm) was used to photoexcite the samples. A cylindrical lens was employed to produce a stripe with defined edges using razor blades. The emission was collected using a lens that was perpendicular to the excitation beam and then fiber-coupled to a CCD through a spectrograph (Princeton) for spectral acquisition, or to a streak camera (Hamamatsu) for time-resolved data collection.

Fluorescence Correlation Spectroscopy. We employed a confocal microscope with pulsed excitation and a Hanbury–Brown–Twiss setup to detect emission from diffusing QSs in solution, and evaluated the second-order cross-correlation function, $g^{(2)}(\tau)$, a technique known as fluorescence correlation spectroscopy (FCS) for solution-based measurements. At early τ, when QDs are still within the probed confocal volume, photon pairs are more likely to originate from the same QS, leading to higher correlation at timescales faster than QS diffusion time. For τ beyond the diffusion time, photon pairs mostly come from different QSs and are not correlated, resulting in $g^{(2)}(\tau)$ comprising uncorrelated photon pairs from the entire ensemble. At $\tau = 0$, the intensity shows a mixture of antibunching from exciton emission, bunching from biexciton emission, and some signal from photon pairs from different QSs. To isolate single QD correlations from the ensemble, we subtract the uncorrelated ensemble emission (large τ) from the dilute sample's highly correlated emission at short timescales (small τ). To obtain the ensemble-averaged BX/X QY, we calculate the ratio of the ensemble background-subtracted correlation center peak ($g^{(2)}(0) - 1$) to the correlation side peak ($g^{(2)}(\tau_{rep}) - 1$), where τ_{rep} is the laser repetition rate. The correlation side peak is determined as described in the Supporting Information. To avoid higher-order multiexciton emission, all measurements were conducted under low excitation flux ($\langle n \rangle \ll 1$), and we ensured that the pulsed laser repetition rate exceeded the emitter's lifetime.

■ ASSOCIATED CONTENT

Supporting Information

The Supporting Information is available free of charge at https://pubs.acs.org/doi/10.1021/jacs.3c03397.

Additional figures, including TEM and STEM images, PL data, single-particle PL dynamics, and theoretical calculations, including model calculations of electron/hole wave functions (PDF)

■ AUTHOR INFORMATION

Corresponding Author

Mikhail Zamkov − *The Center for Photochemical Sciences and Department of Physics, Bowling Green State University, Bowling Green, Ohio 43403, United States;* orcid.org/0000-0002-8638-2972; Phone: 419-372-0264; Email: zamkovm@bgsu.edu; Fax: 419-372-9938

Authors

Dulanjan Harankahage − *The Center for Photochemical Sciences and Department of Physics, Bowling Green State University, Bowling Green, Ohio 43403, United States*

James Cassidy − *The Center for Photochemical Sciences and Department of Physics, Bowling Green State University, Bowling Green, Ohio 43403, United States*

Jacob Beavon − *Department of Physics, Bowling Green State University, Bowling Green, Ohio 43403, United States*

Jiamin Huang − *The Center for Photochemical Sciences and Department of Physics, Bowling Green State University, Bowling Green, Ohio 43403, United States*

Niamh Brown − *Department of Chemistry, Massachusetts Institute of Technology, Cambridge, Massachusetts 02139, United States*

David B. Berkinsky − *Department of Chemistry, Massachusetts Institute of Technology, Cambridge, Massachusetts 02139, United States*

Andrew Marder − *Department of Physics, University of Texas at Dallas, Richardson, Texas 75080, United States;* orcid.org/0000-0002-8981-9762

Barbra Kayira − *Department of Physics, Bowling Green State University, Bowling Green, Ohio 43403, United States*

Michael Montemurri − *Department of Physics, Bowling Green State University, Bowling Green, Ohio 43403, United States*

Pavel Anzenbacher − *The Center for Photochemical Sciences and Department of Chemistry, Bowling Green State University, Bowling Green, Ohio 43403, United States;* orcid.org/0000-0001-8407-1663

Richard D. Schaller − *Center for Nanoscale Materials, Argonne National Laboratory, Lemont, Illinois 60439, United States; Department of Chemistry, Northwestern University, Evanston, Illinois 60208, United States;* orcid.org/0000-0001-9696-8830

Liangfeng Sun − *The Center for Photochemical Sciences and Department of Physics, Bowling Green State University, Bowling Green, Ohio 43403, United States;* orcid.org/0000-0003-0527-1777

Moungi G. Bawendi − *Department of Chemistry, Massachusetts Institute of Technology, Cambridge, Massachusetts 02139, United States;* orcid.org/0000-0003-2220-4365

Anton V. Malko − *Department of Physics, University of Texas at Dallas, Richardson, Texas 75080, United States;* orcid.org/0000-0001-6410-7112

Benjamin T. Diroll − *Center for Nanoscale Materials, Argonne National Laboratory, Lemont, Illinois 60439, United States;* orcid.org/0000-0003-3488-0213

Complete contact information is available at: https://pubs.acs.org/10.1021/jacs.3c03397

Notes

The authors declare no competing financial interest.

■ ACKNOWLEDGMENTS

This work was supported by the Award DE-SC0016872 (M.Z.) funded by the U.S. Department of Energy, Office of Science. The authors acknowledge the financial support of the University of Michigan College of Engineering and NSF grant #DMR-9871177, and technical support from the Michigan Center for Materials Characterization. D.B.B. and N.B. were supported by the U.S. Department of Energy, Office of Basic

Energy Sciences, Division of Materials Sciences and Engineering (Award DE-SC0021650). Work performed at the Center for Nanoscale Materials, a U.S. Department of Energy Office of Science User Facility, was supported by the U.S. DOE, Office of Basic Energy Sciences, under Contract No. DE-AC02-06CH11357. J.B. and M.Z. acknowledge the support by NSF award #2208834. The work of UT Dallas group (A.V.M., Navendu Mondal (NM) and Kehui Zhang (KZ)) was supported by DOE-BES award #DE-SC0010697. P.A. was supported by the National Science Foundation (NSF CHE 2102581).

REFERENCES

(1) Hanifi, D. A.; Bronstein, N. D.; Koscher, B. A.; Nett, Z.; Swabeck, J. K.; Takano, K.; Schwartzberg, A. M.; Maserati, L.; Vandewal, K.; van de Burgt, Y.; Salleo, A.; Alivisatos, A. P. Redefining Near-Unity Luminescence in Quantum Dots with Photothermal Threshold Quantum Yield. *Science* **2019**, *363*, 1199−1202.

(2) Park, Y.-S.; Roh, J.; Diroll, B. T.; Schaller, R. D.; Klimov, V. I. Colloidal Quantum Dot Lasers. *Nat. Rev. Mater.* **2021**, *6*, 382−401.

(3) Shirasaki, Y.; Supran, G. J.; Bawendi, M. G.; Bulović, V. Emergence of Colloidal Quantum-Dot Light-Emitting Technologies. *Nat. Photonics* **2013**, *7*, 13−23.

(4) Yang, J.; Choi, M. K.; Yang, U. J.; Kim, S. Y.; Kim, Y. S.; Kim, J. H.; Kim, D.-H.; Hyeon, T. Toward Full-Color Electroluminescent Quantum Dot Displays. *Nano Lett.* **2021**, *21*, 26−33.

(5) Panfil, Y. E.; Oded, M.; Banin, U. Colloidal Quantum Nanostructures: Emerging Materials for Display Applications. *Angew. Chem., Int. Ed.* **2018**, *57*, 4274−4295.

(6) de Arquer, F. P. G.; Talapin, D. V.; Klimov, V. I.; Arakawa, Y.; Bayer, M.; Sargent, E. H. Semiconductor Quantum Dots: Technological Progress and Future Challenges. *Science* **2021**, *373*, No. eaaz8541.

(7) Lim, J.; Park, Y.-S.; Klimov, V. I. Optical Gain in Colloidal Quantum Dots Achieved with Direct-Current Electrical Pumping. *Nat. Mater.* **2018**, *17*, 42−49.

(8) Klimov, V. I.; Mikhailovsky, A. A.; McBranch, D. W.; Leatherdale, C. A.; Bawendi, M. G. Quantization of Multiparticle Auger Rates in Semiconductor Quantum Dots. *Science* **2000**, *287*, 1011−1013.

(9) Kharchenko, V. A.; Rosen, M. Auger Relaxation Processes in Semiconductor Nanocrystals and Quantum Wells. *J. Lumin.* **1996**, *70*, 158−169.

(10) Nirmal, M.; Dabbousi, B. O.; Bawendi, M. G.; Macklin, J. J.; Trautman, J. K.; Harris, T. D.; Brus, L. E. Fluorescence Intermittency in Single Cadmium Selenide Nanocrystals. *Nature* **1996**, *383*, 802−804.

(11) Bae, W. K.; Park, Y.-S.; Lim, J.; Lee, D.; Padilha, L. A.; McDaniel, H.; Robel, I.; Lee, C.; Pietryga, J. M.; Klimov, V. I. Controlling the Influence of Auger Recombination on the Performance of Quantum-Dot Light-Emitting Diodes. *Nat. Commun.* **2013**, *4*, No. 2661.

(12) Meng, Z.; Mahler, B.; Houel, J.; Kulzer, F.; Ledoux, G.; Vasil′ev, A.; Dujardin, C. Perspectives for CdSe/CdS Spherical Quantum Wells as Rapid-Response Nano-Scintillators. *Nanoscale* **2021**, *13*, 19578−19586.

(13) Wang, J.-X.; Wang, X.; Yin, J.; Gutiérrez-Arzaluz, L.; He, T.; Chen, C.; Han, Y.; Zhang, Y.; Bakr, O. M.; Eddaoudi, M.; Mohammed, O. F. Perovskite-Nanosheet Sensitizer for Highly Efficient Organic X-Ray Imaging Scintillator. *ACS Energy Lett.* **2022**, *7*, 10−16.

(14) Lim, J.; Park, Y.-S.; Wu, K.; Yun, H. J.; Klimov, V. I. Droop-Free Colloidal Quantum Dot Light-Emitting Diodes. *Nano Lett.* **2018**, *18*, 6645−6653.

(15) Fan, F.; Voznyy, O.; Sabatini, R. P.; Bicanic, K. T.; Adachi, M. M.; McBride, J. R.; Reid, K. R.; Park, Y.-S.; Li, X.; Jain, A.; Quintero-Bermudez, R.; Saravanapavanantham, M.; Liu, M.; Korkusinski, M.; Hawrylak, P.; Klimov, V. I.; Rosenthal, S. J.; Hoogland, S.; Sargent, E. H. Continuous-Wave Lasing in Colloidal Quantum Dot Solids Enabled by Facet-Selective Epitaxy. *Nature* **2017**, *544*, 75−79.

(16) Klimov, V. I.; Mikhailovsky, A. A.; Xu, S.; Malko, A.; Hollingsworth, J. A.; Leatherdale, C. A.; Eisler, H.-J.; Bawendi, M. G. Optical Gain and Stimulated Emission in Nanocrystal Quantum Dots. *Science* **2000**, *290*, 314−317.

(17) Padilha, L. A.; Robel, I.; Lee, D. C.; Nagpal, P.; Pietryga, J. M.; Klimov, V. I. Spectral Dependence of Nanocrystal Photoionization Probability: The Role of Hot-Carrier Transfer. *ACS Nano* **2011**, *5*, 5045−5055.

(18) Pinaud, F.; Clarke, S.; Sittner, A.; Dahan, M. Probing Cellular Events, One Quantum Dot at a Time. *Nat. Methods* **2010**, *7*, 275−285.

(19) Ben-Shahar, Y.; Philbin, J. P.; Scotognella, F.; Ganzer, L.; Cerullo, G.; Rabani, E.; Banin, U. Charge Carrier Dynamics in Photocatalytic Hybrid Semiconductor−Metal Nanorods: Crossover from Auger Recombination to Charge Transfer. *Nano Lett.* **2018**, *18*, 5211−5216.

(20) She, C.; Fedin, I.; Dolzhnikov, D. S.; Demortière, A.; Schaller, R. D.; Pelton, M.; Talapin, D. V. Low-Threshold Stimulated Emission Using Colloidal Quantum Wells. *Nano Lett.* **2014**, *14*, 2772−2777.

(21) Kelestemur, Y.; Shynkarenko, Y.; Anni, M.; Yakunin, S.; De Giorgi, M. L.; Kovalenko, M. V. Colloidal CdSe Quantum Wells with Graded Shell Composition for Low-Threshold Amplified Spontaneous Emission and Highly Efficient Electroluminescence. *ACS Nano* **2019**, *13*, 13899−13909.

(22) Guzelturk, B.; Pelton, M.; Olutas, M.; Demir, H. V. Giant Modal Gain Coefficients in Colloidal II−VI Nanoplatelets. *Nano Lett.* **2019**, *19*, 277−282.

(23) Chen, B.; Chang, S.; Li, D.; Chen, L.; Wang, Y.; Chen, T.; Zou, B.; Zhong, H.; Rogach, A. L. Template Synthesis of CuInS 2 Nanocrystals from In 2 S 3 Nanoplates and Their Application as Counter Electrodes in Dye-Sensitized Solar Cells. *Chem. Mater.* **2015**, *27*, 5949−5956.

(24) Diroll, B. T.; Guzelturk, B.; Po, H.; Dabard, C.; Fu, N.; Makke, L.; Lhuillier, E.; Ithurria, S. 2D II−VI Semiconductor Nanoplatelets: From Material Synthesis to Optoelectronic Integration. *Chem. Rev.* **2023**, *123*, 3543−3624.

(25) Kozlov, O. V.; Park, Y.-S.; Roh, J.; Fedin, I.; Nakotte, T.; Klimov, V. I. Sub−Single-Exciton Lasing Using Charged Quantum Dots Coupled to a Distributed Feedback Cavity. *Science* **2019**, *365*, 672−675.

(26) Razgoniaeva, N.; Moroz, P.; Yang, M.; Budkina, D. S.; Eckard, H.; Augspurger, M.; Khon, D.; Tarnovsky, A. N.; Zamkov, M. One-Dimensional Carrier Confinement in "Giant" CdS/CdSe Excitonic Nanoshells. *J. Am. Chem. Soc.* **2017**, *139*, 7815−7822.

(27) Kholmicheva, N.; Budkina, D. S.; Cassidy, J.; Porotnikov, D.; Harankahage, D.; Boddy, A.; Galindo, M.; Khon, D.; Tarnovsky, A. N.; Zamkov, M. Sustained Biexciton Populations in Nanoshell Quantum Dots. *ACS Photonics* **2019**, *6*, 1041−1050.

(28) Nagamine, G.; Jeong, B. G.; Ferreira, T. A. C.; Chang, J. H.; Park, K.; Lee, D. C.; Bae, W. K.; Padilha, L. A. Efficient Optical Gain in Spherical Quantum Wells Enabled by Engineering Biexciton Interactions. *ACS Photonics* **2020**, *7*, 2252−2264.

(29) Cassidy, J.; Diroll, B. T.; Mondal, N.; Berkinsky, D. B.; Zhao, K.; Harankahage, D.; Porotnikov, D.; Gately, R.; Khon, D.; Proppe, A.; Bawendi, M. G.; Schaller, R. D.; Malko, A. V.; Zamkov, M. Quantum Shells Boost the Optical Gain of Lasing Media. *ACS Nano* **2022**, *16*, 3017−3026.

(30) Proppe, A. H.; Lee, K. L. K.; Cortes, C. L.; Saif, M.; Berkinsky, D. B.; Sverko, T.; Sun, W.; Cassidy, J.; Zamkov, M.; Kim, T.; Jang, E.; Gray, S. K.; McGuire, B. A.; Bawendi, M. G. Adversarial Autoencoder Ensemble for Fast and Probabilistic Reconstructions of Few-Shot Photon Correlation Functions for Solid-State Quantum Emitters. *Phys. Rev. B* **2022**, *106*, No. 045425.

(31) Cassidy, J.; Harankahage, D.; Porotnikov, D.; Malko, A. V.; Zamkov, M. Colloidal Quantum Shells: An Emerging 2D Semiconductor for Energy Applications. *ACS Energy Lett.* **2022**, *7*, 1202−1213.

https://doi.org/10.1021/jacs.3c03397
J. Am. Chem. Soc. 2023, 145, 13326−13334

(32) Marder, A. A.; Cassidy, J.; Harankahage, D.; Beavon, J.; Gutiérrez-Arzaluz, L.; Mohammed, O. F.; Mishra, A.; Adams, A. C.; Slinker1, J. D.; Hu, Z.; Savoy, S.; Zamkov, M.; Malko, A. V. CdS/CdSe/CdS Spherical Quantum Wells with Near-Unity Biexciton Quantum Yield for Light-Emitting Device Applications. *ACS Mater. Lett.* **2023**, *5*, 1411−1419.
(33) Pokatilov, E. P.; Fonoberov, V. A.; Fomin, V. M.; Devreese, J. T. Electron and Hole States in Quantum Dot Quantum Wells within a Spherical Eight-Band Model. *Phys. Rev. B* **2001**, *64*, No. 245329.
(34) Dias, E. A.; Saari, J. I.; Tyagi, P.; Kambhampati, P. Improving Optical Gain Performance in Semiconductor Quantum Dots via Coupled Quantum Shells. *J. Phys. Chem. C* **2012**, *116*, 5407−5413.
(35) Braun, M.; Link, S.; Burda, C.; El-Sayed, M. Transfer Times of Electrons and Holes across the Interface in CdS/HgS/CdS Quantum Dot Quantum Well Nanoparticles. *Chem. Phys. Lett.* **2002**, *361*, 446−452.
(36) Xu, J.; Xiao, M. Lasing Action in Colloidal CdS/CdSe/CdS Quantum Wells. *Appl. Phys. Lett.* **2005**, *87*, No. 173117.
(37) Xu, J.; Xiao, M.; Battaglia, D.; Peng, X. Exciton Radiative Recombination in Spherical CdS/CdSe/CdS Quantum-Well Nanostructures. *Appl. Phys. Lett.* **2005**, *87*, No. 043107.
(38) Battaglia, D.; Li, J. J.; Wang, Y.; Peng, X. Colloidal Two-Dimensional Systems: CdSe Quantum Shells and Wells. *Angew. Chem., Int. Ed.* **2003**, *42*, 5035−5039.
(39) Jeong, B. G.; Park, Y.-S.; Chang, J. H.; Cho, I.; Kim, J. K.; Kim, H.; Char, K.; Cho, J.; Klimov, V. I.; Park, P.; Lee, D. C.; Bae, W. K. Colloidal Spherical Quantum Wells with Near-Unity Photoluminescence Quantum Yield and Suppressed Blinking. *ACS Nano* **2016**, *10*, 9297−9305.
(40) Philbin, J. P.; Rabani, E. Electron−Hole Correlations Govern Auger Recombination in Nanostructures. *Nano Lett.* **2018**, *18*, 7889−7895.
(41) Robel, I.; Gresback, R.; Kortshagen, U.; Schaller, R. D.; Klimov, V. I. Universal Size-Dependent Trend in Auger Recombination in Direct-Gap and Indirect-Gap Semiconductor Nanocrystals. *Phys. Rev. Lett.* **2009**, *102*, No. 177404.
(42) Cassidy, J.; Zamkov, M. Nanoshell Quantum Dots: Quantum Confinement beyond the Exciton Bohr Radius. *J. Chem. Phys.* **2020**, *152*, No. 110902.
(43) Cassidy, J.; Harankahage, D.; Ojile, J.; Porotnikov, D.; Walker, L.; Montemurri, M.; Narvaez, B. S. L.; Khon, D.; Forbes, M. D. E.; Zamkov, M. Shape Control of Colloidal Semiconductor Nanocrystals through Thermodynamically Driven Aggregative Growth. *Chem. Mater.* **2022**, *34*, 2484−2494.
(44) Guo, Y.; Marchuk, K.; Sampat, S.; Abraham, R.; Fang, N.; Malko, A. V.; Vela, J. Unique Challenges Accompany Thick-Shell CdSe/NCdS (n > 10) Nanocrystal Synthesis. *J. Phys. Chem. C* **2012**, *116*, 2791−2800.
(45) Beyler, A. P.; Bischof, T. S.; Cui, J.; Coropceanu, I.; Harris, D. K.; Bawendi, M. G. Sample-Averaged Biexciton Quantum Yield Measured by Solution-Phase Photon Correlation. *Nano Lett.* **2014**, *14*, 6792−6798.
(46) Nair, G.; Zhao, J.; Bawendi, M. G. Biexciton Quantum Yield of Single Semiconductor Nanocrystals from Photon Statistics. *Nano Lett.* **2011**, *11*, 1136−1140.
(47) Park, Y.-S.; Lim, J.; Makarov, N. S.; Klimov, V. I. Effect of Interfacial Alloying versus "Volume Scaling" on Auger Recombination in Compositionally Graded Semiconductor Quantum Dots. *Nano Lett.* **2017**, *17*, 5607−5613.
(48) Mangum, B. D.; Sampat, S.; Ghosh, Y.; Hollingsworth, J. A.; Htoon, H.; Malko, A. V. Influence of the core size on biexciton quantum yield of giant CdSe/CdS nanocrystals. *Nanoscale* **2014**, *6*, 3712−3720.
(49) Sampat, S.; Karan, N. S.; Guo, T.; Htoon, H.; Hollingsworth, J. A.; Malko, A. V. Multistate blinking and scaling of the recombination rates in individual silica-coated CdSe/CdS nanocrystals. *ACS Photonics* **2015**, *2*, 1505−1512.
(50) Haus, J. W.; Zhou, H. S.; Honma, I.; Komiyama, H. Quantum Confinement in Semiconductor Heterostructure Nanometer-Size Particles. *Phys. Rev. B* **1993**, *47*, 1359−1365.
(51) Park, Y.-S.; Malko, A. V.; Vela, J.; Chen, Y.; Ghosh, Y.; García-Santamaría, F.; Hollingsworth, J. A.; Klimov, V. I.; Htoon, H. Near-Unity Quantum Yields of Biexciton Emission from CdSe/CdS Nanocrystals Measured Using Single-Particle Spectroscopy. *Phys. Rev. Lett.* **2011**, *106*, No. 187401.
(52) Klimov, V. I.; McGuire, J. A.; Schaller, R. D.; Rupasov, V. I. Scaling of Multiexciton Lifetimes in Semiconductor Nanocrystals. *Phys. Rev. B* **2008**, *77*, No. 195324.
(53) Klimov, V. I.; Ivanov, S. A.; Nanda, J.; Achermann, M.; Bezel, I.; McGuire, J. A.; Piryatinski, A. Single-Exciton Optical Gain in Semiconductor Nanocrystals. *Nature* **2007**, *447*, 441−446.
(54) Kobiyama, E.; Tahara, H.; Sato, R.; Saruyama, M.; Teranishi, T.; Kanemitsu, Y. Reduction of Optical Gain Threshold in CsPbI 3 Nanocrystals Achieved by Generation of Asymmetric Hot-Biexcitons. *Nano Lett.* **2020**, *20*, 3905−3910.
(55) Cassidy, J.; Ellison, C.; Bettinger, J.; Yang, M.; Moroz, P.; Zamkov, M. Enabling Narrow Emission Line Widths in Colloidal Nanocrystals through Coalescence Growth. *Chem. Mater.* **2020**, *32*, 7524−7534.